

# A Comparison of Ultraviolet, Optical, and X-Ray Imagery of Selected Fields in the Cygnus Loop

CHARLES W. DANFORTH<sup>1</sup>, ROBERT H. CORNETT<sup>2</sup>, N. A. LEVENSON<sup>1</sup>, WILLIAM P. BLAIR<sup>1</sup>,  
THEODORE P. STECHER<sup>3</sup>

Accepted for Publication January 27, 2000

## ABSTRACT

During the Astro-1 and Astro-2 Space Shuttle missions in 1990 and 1995, far ultraviolet (FUV) images of five 40' diameter fields around the rim of the Cygnus Loop supernova remnant were observed with the Ultraviolet Imaging Telescope (UIT). These fields sampled a broad range of conditions including both radiative and nonradiative shocks in various geometries and physical scales. In these shocks, the UIT B5 band samples predominantly C IV  $\lambda 1550$  and the hydrogen two-photon recombination continuum. Smaller contributions are made by emission lines of He II  $\lambda 1640$  and O III]  $\lambda 1665$ . We present these new FUV images and compare them with optical H $\alpha$  and [O III], and ROSAT HRI X-ray images. Comparing the UIT images with those from the other bands provides new insights into the spatial variations and locations of these different types of emission. By comparing against shock model calculations and published FUV spectroscopy at select locations, we surmise that resonance scattering in the strong FUV permitted lines is widespread in the Cygnus Loop, especially in the bright optical filaments typically selected for observation in most previous studies.

*Subject headings:* ISM: nebulae — ISM: supernova remnants — ISM: shock waves — ultraviolet: imaging

## 1. Introduction

Because of its large angular size and wide range of shock conditions, the Cygnus Loop is one of the best laboratories for studying the environment and physics of middle-aged supernova

---

<sup>1</sup>Department of Physics and Astronomy, The Johns Hopkins University, 3400 N. Charles Street, Baltimore, MD 21218; danforth@pha.jhu.edu, levenson@pha.jhu.edu, wpb@pha.jhu.edu

<sup>2</sup>Raytheon ITSS, 4400 Forbes Blvd., Lanham, MD 20706; cornett@stars.gsfc.nasa.gov

<sup>3</sup>Laboratory for Astronomy and Solar Physics, NASA/GSFC, Code 681, Greenbelt, MD 20771; stecher@stars.gsfc.nasa.gov

remnants (SNR). It covers a huge expanse in the sky ( $2.8 \times 3.5^\circ$ ) corresponding to  $21.5 \times 27$  pc, at a newly determined distance of 440 pc (Blair et al. 1999). The currently accepted view for the Cygnus Loop is that it represents an explosion in a cavity produced by a fairly massive precursor star (cf. Levenson et al. 1998). The SN shock has been traveling relatively unimpeded for roughly ten parsecs and has only recently begun reaching the denser cavity walls. The size of the cavity implicates a precursor star of type early B. The interaction of the shock with the complex edges of the cavity wall is responsible for the complicated mixture of optical and X-ray emission seen in superposition, and a dazzling variety of optical filament morphologies.

Portions of the SN blast wave propagating through the fairly rarefied atomic shell ( $< 1 \text{ cm}^{-3}$ ), show faint filaments with hydrogen Balmer-line-dominated optical spectra. These filaments represent the position of the primary blast wave and are often termed nonradiative shocks (because radiative losses are unimportant to the dynamics of the shock itself). Ambient gas is swept up and progressively ionized, emitting He II, C IV, N V, and O VI lines in the FUV (Figure 1, bottom spectrum) (Hester, Raymond, & Blair 1994, Raymond et al. 1983). Balmer-dominated emission arises from the fraction ( $\sim 0.3$ ) of neutral hydrogen swept up by the shock that stands some chance of being excited and recombining before it is ionized in the post-shock flow (Chevalier & Raymond 1978; Chevalier, Kirshner, & Raymond 1980).

The Balmer emission is accompanied by hydrogen two-photon events which produce a broad continuum above  $1216\text{\AA}$  peaking at  $\sim 1420\text{\AA}$  (Nussbaumer & Schmutz 1984). For recombination and for high temperature shocks, the ratio of two-photon emission to Balmer is nearly constant ( $\sim 8:1$ ). In slow shocks ( $\sim 40 \text{ km s}^{-1}$ ) in neutral gas, the ratio can be enhanced considerably (Dopita, Binette, & Schwartz, 1982).

Balmer-dominated filaments are very smooth and WFPC2 observations by Blair et al. (1999) show that they are exceedingly thin as well—less than one WFC pixel across when seen edge-on, or  $< 6 \times 10^{14}$  cm at our assumed distance, in keeping with theoretical predictions (cf. Raymond et al. 1983). Postshock temperatures reach millions of degrees and the hot material emits copious soft X-rays. The density is low, however, and cooling is very inefficient. With time, as the shock continues to sweep up material, these filaments will be able to start cooling more effectively and will evolve to become radiative filaments.

The bright optical filaments in the Cygnus Loop represent radiative shocks in much denser material, such as might be expected in the denser portions of the cavity wall. These shocks are said to be radiative (that is, energy losses from radiation are significant); they have more highly developed cooling and/or recombination zones. The shocked material emits in the lines of a broad range of hot, intermediate, and low temperature ions, depending on the effective ‘age’ of the shock at a given location and the local physical conditions. For instance, a relatively recent encounter between the shock and a density enhancement (or similarly, a shock that has swept up a fairly low total column of material) may show very strong [O III]  $\lambda 5007$  compared with  $H\alpha$ . This would indicate that the coolest part of the flow, the recombination zone where the Balmer lines become

strong, has not yet formed. Such shocks are said to be ‘incomplete’ as the shocked material remains hot and does not yet emit in the lower ionization lines.

In contrast, radiative filaments with the full range of ionization (including the low ionization lines) are well approximated by full, steady-flow shock model calculations, such as those of Raymond (1979), Dopita, Binette, & Tuohy (1984), and Hartigan, Raymond, & Hartmann (1987; hereafter HRH). Morphologically, radiative complete filaments lack the smooth grace of nonradiative filaments or even radiative incomplete filaments in some cases (cf. Fesen, Blair, & Kirshner 1982). The more irregular appearance of these filaments is due partly to inhomogeneities in the shocked clouds themselves, partly to turbulence and/or thermal instabilities that set in during cooling (cf. Innes (1992) and references therein), and partly to several clouds appearing along single lines of sight. Often the emission at a given filament position cannot be characterized by a single shock velocity.

Much of the above understanding of shock types and evolutionary stages has been predicated on UV/optical studies of the Cygnus Loop itself. The Cygnus Loop is a veritable laboratory for such studies because of its relative proximity, large angular extent and low foreground extinction ( $E[B - V] = 0.08$ ; Fesen, Blair, & Kirshner 1982), and thus its accessibility across the electromagnetic spectrum. However, because of the range of shock interactions and shock types, coupled with the significant complication of projection effects near the limb of the SNR, great care must be taken in order to obtain a full understanding of what is happening at any given position in the nebular structure.

Although FUV spectra are available at a number of individual filament locations from years of observations with IUE and the shuttle-borne Hopkins Ultraviolet Telescope (HUT), the perspective obtainable from FUV imaging has been largely lacking. The Ultraviolet Imaging Telescope (UIT) was flown as part of the Astro-1 Space Shuttle mission in 1990 was used to observe a field in the Cygnus Loop through both mid-UV and far-UV (FUV) filters (Cornett et al. 1992). In this paper, we report on additional FUV observations with UIT obtained during the Astro-2 shuttle mission in 1995. In addition to the field imaged during Astro-1, UIT observed four different regions around the periphery of the Cygnus Loop with a resolution comparable to existing optical and X-ray observations. These fields sample the full range of physical and shock conditions and evolutionary stages in the SNR. We combine these data with existing ground-based optical images and ROSAT HRI X-ray data to obtain new insights into this prototypical SNR and its interaction with its surroundings.

In §2 we present the observations obtained with the UIT and review the comparison data sets. In §3 we discuss the spectral content of the UIT filter used in the observations. In §4 we discuss examples of the various kinds of shocks as seen in the UIT fields, and summarize our conclusions in §5.

## 2. UIT Observations and Comparison Data

UIT has flown twice on the Space Shuttle as part of the Astro-1 and Astro-2 programs (1990 December 2-10 and 1995 March 2-18). Together with the Hopkins Ultraviolet Telescope (HUT) and the Wisconsin Ultraviolet Photo-Polarimeter Experiment, UIT explored selected UV targets. An f/9 Ritchey-Chretien telescope with a 38 cm aperture and image intensifier systems produced images of circular 40' fields of view with  $\sim 3''$  resolution at field center (depending on pointing stability). Images were recorded on 70mm Eastman Kodak IIA-O film which was developed and digitized at NASA/GSFC and processed into uniform data products. Technical details on the hardware and data processing can be found in Stecher et al. (1992) and Stecher et al. (1997).

Table 1: UIT B5 Filter Observations in the Cygnus Loop

Position	RA(J2000)	Dec(J2000)	exposure (sec)	Figure
W cloud	20:45:38	+31:06:33	1010	3
NE nonrad	20:54:39	+32:17:29	2041	4
NE cloud	20:56:16	+31:44:34	500	5
XA region <sup>a</sup>	20:57:35	+31:07:28	1280	6
XA region	20:57:04	+31:07:45	1151	6
XA region	20:57:22	+31:04:02	1516	6
XA region	20:57:24	+31:03:51	1274	6
SE cloud	20:56:05	+30:44:01	2180	7

<sup>a</sup> Astro-1 image (cf. Cornett et al. 1992)

Astro/UIT images are among the few examples of FUV images of SNRs, and UIT's B5 bandpass ( $\sim 1450\text{\AA}$  to  $\sim 1800\text{\AA}$ ) encompasses severally generally high-excitation and heretofore unmapped lines that are often present in SNR shocks (Figure 1). UIT's two Astro flights have produced eight FUV images of five different Cygnus Loop fields. Table 1 lists the observation parameters and field locations, which are indicated in Figure 2. We will refer to these fields by the names listed in Table 1. Since all four exposures of the XA region (named by Hester & Cox 1986) are reasonably deep, we constructed a mosaic of the field using the IRAF<sup>4</sup> IMCOMBINE task, resulting in significantly improved signal-to-noise in the overlapped region of the combined image. In panel c of Figures 3 through 7, we show the five reduced UIT images as observed in the B5 filter bandpass.

UIT images with long exposure times suffer from an instrumental malady dubbed "measles" by the UIT team (Stecher et al. 1997). Measles manifest themselves as fixed-pattern noise spikes in images with a large sunlight flux, such as long daylight exposures or images of red, very bright sources (e.g. planets or the Moon). This effect is probably produced by visible light passing

---

<sup>4</sup>IRAF is distributed by the National Optical Astronomy Observatories, which is operated by the Association of Universities for Research in Astronomy, Inc. (AURA) under cooperative agreement with the National Science Foundation.

through pinholes in either the output phosphor of the first stage or the bialkali photocathode of the second stage of the UIT FUV image tube. The Cygnus Loop was a daytime object for both the Astro-1 and Astro-2 flights, but the phenomenon is visible only in some of the longer exposures. Most dramatically, measles are seen in the northeast cloud nonradiative image (Figure 4) as a darkening in the northwest corner; the individual “measles” are spread into a background by the binning used to produce these images. Various approaches to removing the appearance of measles were attempted but none of them have yielded satisfactory results. In practice, the measles, here arising from daylight sky contamination, affect our analysis only by adding to the background level, so the original images are presented here, “measles” and all.

For comparison with our FUV images, we show narrow-band optical images in [O III]  $\lambda 5007$  and  $H\alpha + [N II]$  (which for simplicity we refer to as  $H\alpha$ ) obtained with the Prime Focus Corrector on the 0.8 m telescope at McDonald Observatory (cf. Levenson et al. 1998). These images, shown in panels a and b of Figures 3 – 7, are aligned and placed on a common scale of  $5''$  per pixel, which is similar to the FUV resolution of  $3''$ . The optical images have each been processed with a 3-pixel median filter to remove faint stars and stellar residuals.

In addition, we show the soft X-ray (0.1–2.4 keV) emission for each field, as observed with the *ROSAT* High Resolution Imager (HRI) (from Levenson et al. 1997). The resolution of the HRI imager is  $6''$  on axis degrading to  $30''$  at the edge of each field. As with the optical data, the X-ray images are aligned on a  $5''$  per pixel scale. The HRI images have additionally been smoothed with a 3-pixel FWHM gaussian and are shown in panel d of Figures 3 – 7. All images in Figures 3 – 7 are displayed on a logarithmic scale.

Figure 8 shows three-color composite images using  $H\alpha$  as red, B5 as green, and the *ROSAT* HRI as blue. The color levels have been adjusted for visual appearance, to best show the relative spatial relationships of the different emissions. (The color composite for the Northeast nonradiative region is not shown, since little new information is gained above Figure 4 and because of the adverse effect of the measles.) This will be discussed in more detail below.

### 3. Spectral Content of UIT Images

Figure 1 shows the UIT B5 filter profile superimposed on spectra of typical radiative and nonradiative filaments, as observed by HUT. Unlike typical SNR narrow band images in the optical, the B5 filter is relatively broad and does not isolate a single spectral line, but rather encompasses several strong, moderately high ionization lines that are variable from filament to filament. Cornett et al. (1992) point out that C IV should dominate emission in this bandpass since it is a strong line centered near the filter’s peak throughput, and since shock models predict this result for a range of important velocities (cf. Figure 10 and accompanying discussion). Here we look at this more closely over a larger range of shock velocities, and in particular also discuss the potential complicating effects of hydrogen two-photon recombination continuum emission,

shock completeness, and resonance line scattering.

Empirical comparisons of IUE and HUT emission line observations can be used to quantify at what level the C IV emission is expected to dominate the line emission detected through the B5 filter. For instance, in the highly radiative XA region (see Figure 7) we have compared a large number of FUV spectra both on and adjacent to bright optical filaments against the throughput curve of B5 (Danforth, Blair, & Raymond 2000; henceforth DBR). This comparison shows that on average the various lines contribute as follows: C IV  $\lambda 1550$ , 42%; O III]  $\lambda 1665$ , 27%; He II  $\lambda 1640$ , 17%; N IV  $\lambda 1486$ , 8%; and 6% from fainter emission lines. Using the HUT observation of Long et al. (1992), we estimate for nonradiative shocks the B5 contributions are more like C IV (60%), He II (28%), and all other species 12%. These percentages are only approximate, of course, and will vary with shock velocity, geometry and a host of other conditions, but they serve to highlight the fact that, while C IV is the strongest contributor to the line emission, it is not the only contributor.

In addition, while it is not obvious at the scale of Figure 1, a low level continuum is often seen in IUE and HUT spectra of Cygnus Loop filaments, especially where optical  $H\alpha$  emission is present and strong. This continuum arises due to the hydrogen two-photon process (cf. Osterbrock 1989). Benvenuti, Dopita, & D’Odorico (1980) note that SNR shocks cause two-photon emission from hydrogen via both collisional excitation and recombination into the  $2^2S_{1/2}$  state. The two-photon spectrum arises from a probability distribution of photons that is symmetric about 1/2 the energy of  $Ly\alpha$  (corresponding to  $2431\text{\AA}$ ), resulting in a shallow spectral peak near  $1420\text{\AA}$  and extending from  $1216\text{\AA}$  towards longer wavelengths, throughout the UV and optical region. The expected (integrated) strength of this component is about  $8 \times$  the  $H\alpha$  flux but is spread over thousands of Angstroms. However, the wide bandpass of the B5 filter detects  $\sim 15\%$  of the total two-photon flux available, enough to compete with line emission in the bandpass. Further complicating the question, two-photon emission can also be highly variable from filament to filament.

By using signatures from the images and spectra at other wavelengths, we can interpret, at least qualitatively, what is being seen in the UIT images. For instance, Figure 4 shows the NE rim of the SNR. The faint, smooth  $H\alpha$  filament running along the edge of the X-ray emission is clearly a nonradiative filament. The faint emission seen in the B5 image traces these faint Balmer filaments well, and at this position, does not correlate particularly well with the clumpy [O III] emission seen near the middle of the field. This implies a relatively strong contribution from two-photon continuum, although as shown in the bottom spectrum of Figure 1, C IV and He II are also present in the filaments at some level.

As discussed earlier, in radiative filaments, higher ionization lines such as O VI  $\lambda 1035$ , N V  $\lambda 1240$ , C IV  $\lambda 1550$ , and [O III]  $\lambda 5007$  become strong first, followed by lower ionization lines like [S II]  $\lambda 6725$ , [O I]  $\lambda 6300$ , and the hydrogen Balmer lines. Hence, in filaments that show high optical [O III] to  $H\alpha$  ratios, and are thus incomplete shocks, the B5 content primarily arises from C IV and other line emission. In older, more complete shocks where the optical [O III] to  $H\alpha$  ratios

are close to those expected from steady flow shock models, two-photon emission again should compete with the line emission and the B5 flux should arise from both sources. It is difficult to assess these competing effects from Figures 3 – 7 since the relative intensities of the two optical images are not always obvious, but much of the variation in coloration in Figure 8 for bright radiative filaments is due to the variation in relative amounts of line emission and two-photon continuum contributions to the B5 image.

In Figure 9, we show the XA field as seen with UIT (panel a) and ratio maps of the UIT image against the aligned optical  $H\alpha$  and [O III] images. Since the ionization energies of C IV (64.5 eV) and O III (54.9 eV) are similar (and to the extent that the B5 image contains a substantial component of C IV emission), we would expect a ratio of B5 to  $H\alpha$  to show evidence for the transition from incomplete to complete shock filaments. Such a ratio map is shown in panel b of Figure 9, and a systematic pattern is indeed seen. The white filaments, indicative of a relatively low value of the ratio (and hence relatively strong  $H\alpha$  filaments) tend to lie systematically to the right. These filaments tend to be closer to the center of the SNR, and hence should have had more time (on average) to cool and recombine. Of course, there is significant evidence for projection effects in this complicated field as well. Indeed, one interpretation of Figure 9b is that we are separating some of these projection effects, and are seeing two separate ‘systems’ of filaments that are at differing stages of completeness.

Another way of assessing the expected contributions of line emission and two-photon emission to the B5 flux is by comparing to shock model calculations. We use the equilibrium preionization “E” series shock models of Hartigan, Raymond, & Hartmann (1987, HRH) to investigate variations in spectral contributions to the UIT images as a function of shock velocity. Figure 10 shows how various spectral components are predicted to change in relative intensity as shock velocity increases for this set of planar, complete, steady flow shock models. As expected, the key contributors to the B5 bandpass are indeed C IV and two-photon continuum, although between  $\sim 100 - 200 \text{ km s}^{-1}$  these models indicate C IV should dominate.

This is quite at odds with ‘ground truth’, as supplied by careful comparisons at the specific locations of IUE and HUT spectra within the UIT fields of view. We note that the two-photon flux per  $\text{\AA}$  in HUT and IUE spectra is low and thus difficult to measure accurately since background levels are poorly known. Even so, it is quite clear from comparisons such as those of Benvenuti, Dopita, & D’Odorico (1980) and Raymond et al. (1988) that nowhere do we see C IV dominate at the level implied by Figure 10. (Indeed such studies indicate that two-photon should dominate! As will be discussed more thoroughly in §4, Benvenuti, Dopita, & D’Odorico (1980) and others give two-photon fluxes which overwhelm C IV in the B5 band by a factor of 5-10. Interestingly, consideration of incompleteness effects only serves to exacerbate this discrepancy since the expected two-photon emission should be weaker or absent. Something else is going on.

That ‘something else’ is apparently resonance line scattering. It has long been suspected that the strong UV resonance lines, like N V  $\lambda 1240$ , C II  $\lambda 1335$ , and C IV  $\lambda 1550$ , are affected

by self-absorption along the line of sight, either by local gas within the SNR itself or by the intervening interstellar medium. We can expect significant column depth from the cavity wall of the remnant itself. Since filaments selected for optical/UV observation have tended to be bright, and since many such filaments are edge-on sheets of gas with correspondingly high line of sight column densities (Hester 1987), the spectral observations are likely affected in a systematic way.

While this has been known for some years (Raymond et al. 1981), the UIT data presented here indicate just how widespread resonance line scattering is in the Cygnus Loop and how significantly the C IV intensity may be reduced by this effect. Figure 9c shows a ratio map of the B5 image to the [O III] optical image of the XA region (cf. Cornett et al. 1992). Since [O III] is a forbidden transition, its optically thin emission is not affected by resonance scattering. The ionization potentials for C IV and [O III] are similar, so this ratio should provide some information about resonance scattering, if a significant fraction of the B5 image can be attributed to C IV. Hence, this ratio image shows where resonance line scattering is most important, and provides information on the 3-dimensional structure of regions within the SNR.

The B5 image gives the *appearance* of smaller dynamic range and lower spatial resolution than [O III] because we see optically thick radiation from only a short distance into the filaments. The highest saturation (lowest ratios, or light areas in Figure 9c) occurs in the cores of filaments and dense clouds, such as the three regions indicated in Figure 9a. The “spur” filament was studied in detail by Raymond et al. 1988 and is probably an edge-on sheet of gas. The region marked ‘B’ is the turbulent, incomplete shocked cloud observed with HUT during Astro-1 (Blair et al. 1991). The XA region is also a shocked cloud or finger of dense gas that is likely elongated in our line of sight (cf. Hester & Cox 1986; DBR). What is surprising, however, is the extent to which the light regions in Figure 9c extend beyond the cloud cores into regions of more diffuse emission. This indicates that significant resonance scattering is very widespread in the Cygnus Loop. The diminished C IV flux also boosts the relative importance of two-photon emission in the B5 bandpass and explains the discrepancy between numerous spectral observations and the shock model predictions shown in Figure 10.

UIT’s B5 images are particularly useful in that they sample two important shock physics regimes—the brightest radiative shocks arising in dense clouds and the primary blast wave at the edge of the shell. However, it is evidently difficult to predict the spectral content of B5 images alone without detailed knowledge of the physics of the emitting regions. Nonetheless, B5 images are useful in combination with [O III] $\lambda$ 5007 and H $\alpha$  images as empirical tools. The image combinations allow us to determine whether C IV or two-photon dominates, in two clear-cut cases. 1) In regions where B5 images closely resemble [O III] images, the B5 filter is detecting radiative shocks with velocities in the range 100-200 km s<sup>-1</sup> and therefore primarily C IV. 2) In regions where B5 images closely resemble H $\alpha$ , the B5 filter is detecting largely two-photon emission from recombination of hydrogen in radiative shocks or from collisional excitation of hydrogen in nonradiative shocks.



## 4. Discussion

Each of the fields in our study portrays a range of physical conditions and geometries, and hence filament types, seen in projection in many cases. By comparing the UV, X-ray and optical emissions, we can gain new insights into these complexities. In this section, we discuss the spatial relationships between the hot, intermediate and cooler components seen in these images.

### 4.1. The Western Cloud

In the Western Cloud field (Figure 3) the B5 image of the bright north-south filaments resembles the  $[\text{O III}]5007\text{\AA}$  images very closely. The filaments are clearly portions of a radiative shock viewed edge-on to our line of sight. The Western Cloud has been studied spectroscopically at optical wavelengths by Miller (1974) and in the FUV by Raymond et al. (1980b).

This region shows a case where a cloud is evidently being overrun by a shock, and the cloud is much larger than the scale of the shock. The cloud is elongated in the plane of the sky of dimensions perhaps  $1 \times 10$  pc (Levenson et al. 1998) and represents an interaction roughly 1000 years old (Levenson et al. 1996). The main north-south radiative filament is bright in all wavelengths, with good detailed correlation between B5 and  $[\text{O III}]$ .  $\text{H}\alpha$  is seen to extend farther to the east, toward the center or 'behind' the shock, as is expected in a complete shock stratification.

Bright X-rays (Figure 3d) are seen to lag behind the radiative filaments by  $1-2'$  (0.15 to 0.3 pc). This is indicative of a reverse shock being driven back into the interior material from the dense cloud. This doubly-shocked material shows enhanced brightness of about a factor of 2. From this, Levenson et al. (1996) derive a cloud/ambient density contrast of about 10.

Attempts to fit shock models to optical observations of the bright filament have been frustrated by the large  $[\text{O III}]/\text{H}\beta$  ratio. A shock velocity of  $130 \text{ km s}^{-1}$  was found by Raymond et al. (1980b) using IUE line strengths and assuming a slight departure from steady flow and depleted abundances in both C and Si. Raymond et al. (1980b) also note that much of the hydrogen recombination zone predicted by steady flow models is absent, implying that the interaction is fairly young.

As seen in the  $\text{H}\alpha$  image, a Balmer-dominated filament projects from the south of the bright radiative filament toward the northwest. Raymond et al. (1980a) find that the optical spectrum of the filament contains nothing but hydrogen Balmer lines. High-resolution observations of the  $\text{H}\alpha$  line (Treffers 1981) show a broad component and a narrow component, corresponding to the pre- and post-shock conditions in the filament, with a resulting estimated shock velocity of  $130-170 \text{ km s}^{-1}$ . The filament may be a foreground or background piece of the blast wave not related to the radiative portion of the shock, or a related piece of blast wave that is travelling through the atomic (rather than molecular) component. It is visible in both  $\text{H}\alpha$  (Figure 3a) and B5 (Figure 3c) though generally not in other bands; thus the B5 flux for this filament arises primarily from the

two-photon process. There is a small segment of the filament visible in [O III] where the shock may be becoming radiative, visible in B5 as a brightening near the southern end of the filament.

The X-ray luminosity behind this nonradiative filament is much fainter than that observed to the east of the main radiative filament, since there is no reverse shock associated with the nonradiative filament to boost the brightness (Hester, Raymond, & Blair 1994). The absence of X-rays to the west of this filament confirms that it represents the actual blast front. As expected, the peak X-ray flux lags behind the H $\alpha$  and B5 flux by roughly one arcminute (0.1 pc). This representing the “heating time” of gas behind the shock.

A CO cloud is seen just to the south of the Western Cloud field (Scoville et al. 1977). The presence of CO clearly indicates material with molecular hydrogen at densities of 300-1000 cm $^{-3}$ . The nonradiative filament runs closely along the  $T_{antenna}=5\text{K}$  contour of the CO cloud, indicating this shock is moving through the atomic component at this stage, but showing no sign of interaction with the molecular cloud.

#### 4.2. Northeast Nonradiative Region

The canonical example of nonradiative filaments in any context lies on the north and northeast rim of the Cygnus Loop. There, smooth Balmer filaments extend counterclockwise from the northern limb (Figure 4), and can be seen prominently in H $\alpha$  in Figure 5a. Small portions of this shock system have been extensively studied by Raymond et al. (1983), Blair et al. (1991), Long et al. (1992), Hester, Raymond & Blair (1994), and most recently by Blair et al. (1999). The filaments are clearly visible in H $\alpha$  (Figure 4a) as well as B5 (Figure 4c), but invisible along most of their length in [O III] (Figure 4b) except for small segments. These segments represent portions of the shock front where a slightly higher density has allowed the shock to become partially radiative. The shocked,  $T\sim 10^6\text{K}$  gas emits in an edge-brightened band of X-rays (Figure 4d). The brightness variations in X-rays confirm that the nonradiative filaments are simply wrinkles in the blast wave presenting larger column densities to our line of sight.

Spectroscopic observations of selected locations on the filaments indicate that the B5 filter observes nonradiative filaments as a mixture of C IV and two-photon emission. Long et al. (1992) find an intrinsic ratio of two-photon emission to C IV of 4.3, which gives an observed ratio in B5 of 0.65. Raymond et al. (1983) find fluxes in the same filament which give an observed ratio of 1.6; in a nearby filament, Hester, Raymond & Blair (1994) find a ratio near 2.0. These filaments all have velocities of around 170 km s $^{-1}$ . It is likely that much of the ISM carbon is locked up in grains in the preshock medium, thus boosting the ratio.

The system of thin filaments in the NE nonradiative field extends to the south and is visible in H $\alpha$  ahead of the radiative Northeast Cloud (Figure 5) discussed below.

### 4.3. The Northeast Cloud

The Northeast Cloud (Figure 5) radiative filaments, south and east of the field discussed above, make up one of the brightest systems in the Cygnus Loop. The interaction of the SN blast wave and the denser cavity wall is most evident at this location. A complex of radiative filaments can be seen, apparently jumbled together along our line of sight, displaying the signs of a complete shock undergoing radiative cooling. The X-ray edge marking the SN blast wave is well separated from the optical and UV filaments, implying a strongly decelerated shock and cooling that has continued for some time. Stratification of different ionic species is evident, with [O III] in sharp filaments to the east, and more diffuse H $\alpha$  behind (Figure 8b).

The Northeast Cloud extends into the southern portions of the NE nonradiative field (Figure 4) as well. However, the exposure time for this FUV image is a factor of four shorter than that in Figure 4c, so the nonradiative filaments are not detected above the background. There are a few UV-bright sections which correspond closely with bright [O III] knots. However, other equally bright [O III] knots in the region do not have corresponding FUV knots. This may be evidence for a range of shock velocities, or it may be portions of the shocks that are in transition from nonradiative to radiative conditions.

Using IUE spectra Benvenuti, Dopita, & D’Odorico (1980) measure the two-photon continuum for one of the brightest radiative positions within the NE cloud, with a resulting observed two-photon/C IV ratio of 5.0. Observations of other radiative regions both in the Cygnus Loop and in other SNRs similar in morphology and spectrum give ratios between 1.7 and 10 (Raymond et al. 1988; various unpublished data). Therefore, while conditions vary widely within these shocked regions, spectroscopy indicates that resonance scattering of C IV causes us to see 2-6 times more flux from two-photon emission than from other ions in the field. Yet the B5 morphology of most of the field resembles [O III] far more than H $\alpha$ , as we would expect if two-photon emission were dominant. The apparent conflict is likely caused by the fact that most lines of sight through this region undoubtedly encounter material with a broad range of physical conditions. Furthermore, the UIT NE cloud exposure is the shortest of our set. Only regions bright in both H $\alpha$  and [O III] show up in B5.

### 4.4. The XA Field

The XA field (Figure 6) is a complicated region of predominantly radiative filaments, noteworthy because an extremely bright and sharp X-ray edge corresponds closely to a bright knot of UV/visible emission (Hester & Cox 1986). Indeed, this region is seen to be bright in many wavelengths including radio (Green 1990; Leahy et al. 1997) and infrared (Arendt, Dwek, & Leisawitz 1992). Strong O VI  $\lambda$ 1035 emission is seen (Blair et al. 1991) as well as other high-ionization species; N V, C IV, O III] (DBR) and [Ne V] (Szentgyorgyi et al. 2000). See DBR for a more detailed analysis of this region.

In general, the B5 emission corresponds closely to optical [O III]. However, while optical images show a high contrast between the brightest ‘cloud’ regions and others in ‘empty’ space, B5 contrast is lower (Cornett et al. 1992). This suggests contributions from a high column depth of diffuse C IV and/or two-photon emission. We are either looking at diffuse material through the edge of a cavity wall or are seeing emission from face on sheets of gas. DBR show evidence that the bright ‘cloud’ in the center is not isolated and may be a density enhancement in the cavity wall or a finger of denser material projecting in from the east. The entire blast wave in the region appears indented from the otherwise circular extent of the SNR (Levenson et al. 1997) implying that the disturbance is produced by a cloud extended several parsecs in our line of sight. The visible structure is likely the tip of a much larger cloud.

Levenson et al. (1998) suggest a density enhancement in the cavity wall, resulting in rapid shock deceleration and accounting for the bright emission. IUE and HUT observations show evidence for a  $150 \text{ km s}^{-1}$  cloud shock in the dense core of XA itself (the west-pointing V shape in the center of the field) and a faster, incomplete shock in the more diffuse regions to the north and south (DBR). Two parallel, largely east-west filaments are seen flanking the central ‘cloud’. The X-ray emission is seen to drop off dramatically south of the two long radial filament systems.

Blair et al. (1991) report HUT observations of a radiative but incomplete cloud shock directly to the north of XA marked ‘B’ in Figure 9a. This region features almost complete cooling with the exception of  $H\alpha$  and cooler ions. Raymond et al. (1988) studied the Spur filament and found a completeness gradient along the length of it. This filament is well-defined in B5 as well as the optical bands.

The XA region is the one region in the Cygnus Loop where preionization is visible ahead of the shock front (Levenson et al. 1998). This preionization is caused by X-ray flux from the hot, postshock gas ionizing neutral material across the shock front. The emission measure is high enough in this photoionized preshock gas that it is clearly visible as a diffuse patch of emission a few arc minutes to the east of the main XA knot in the center of the field in both  $H\alpha$  and B5. The B5 flux presumably arises almost entirely from two-photon emission in this case since no [O III] is seen (and hence no strong UV line emission is expected).

One unique ability of the B5 filter becomes apparent in the XA region; that of detecting nonradiative shocks in ionized gas. In the X-ray (Figure 6d) we see a bulge of emission to the north and east of the brightest knot (Hester & Cox’s XA region proper). This bulge does not show up in either of the optical bands, but the perimeter is visible in the FUV at the edge of the X-ray emission in Figure 6c. This region has likely been ionized by X-ray flux from the hot post-shock gas. A nonradiative shock is now propagating through it and, lacking a neutral fraction to radiate in  $H\alpha$ , is seen only in high ions such as C IV. This filament is becoming more complete in its southern extremity (the ‘B’ location in Figure 9a) and is emitting in [O III] as well. This filament also appears to connect to the nonradiative filament seen in  $H\alpha$  in the Northeast cloud (Figure 5a).

#### 4.5. The Southeast Cloud

The Southeast Cloud (Figure 7) presents an interesting quandry. In the optical it appears as a small patch of radiative emission with a few associated nonradiative filaments. Fesen, Kwitter, & Downes (1992) hypothesize that it represents a small, isolated cloud at a late stage of shock interaction. Indeed, the resemblance to the late-stage numerical models of Bedogni & Woodward (1990) and Stone & Norman (1992) is striking.

More recent X-ray analysis (Graham et al. 1995) suggests that the shocked portion of the southeast cloud is merely the tip of a much larger structure. Indeed, it is probably similar to the Western and Northeastern Clouds but at an even earlier point in its evolution. Fesen, Kwitter, & Downes (1992) note that the age of the interaction is probably  $4.1 \times 10^3$  years based on an assumed blast wave velocity. Given the revised distance estimate of Blair et al. (1999), this age becomes  $2.3 \times 10^3$  years.

In  $H\alpha$  (Figure 7a) we see a set of nonradiative filaments to the southeast of the cloud. These filaments are visible very faintly in B5 (Figure 7c) as well. Given the complete lack of X-ray emission (Figure 7d) to the east, these filaments are the primary blast wave. The fact that these filaments are indented from the circular rim of the SNR implies the blast wave is diffracting around some object much larger than the visible emission and extended along our line of sight (Graham et al. 1995).

Fesen et al. identify a filament segment seen to the west of the SE cloud—visible in both  $H\alpha$  and our B5 image—as a reverse shock driven back into the shocked medium. The X-ray emission, however, demonstrates that this is instead due the primary forward-moving blast wave. X-ray enhancement is seen to the west of the cloud, not the east as we would expect from a doubly shocked system. Furthermore, the optical filament is Balmer-dominated, which requires a significant neutral fraction in the pre-shock gas, which would not occur at X-ray producing temperatures (Graham et al. 1995). These points suggest that the filament segment seen is a nonradiative piece of the main blast wave not obviously related to the other emission in the area. The relative faintness and lack of definition compared to other nonradiative filaments suggests that it is not quite parallel to our line of sight.

Meanwhile, the densest material in the shocked cloud tip has cooled enough to emit in ionic species like [O III] (Figure 7b) and C IV. Gas stripping resulting from instabilities in the fluid flow along the edges of the cloud is seen as ‘windblown streamers’ on the north and south as well as diffuse emission (because of a less favorable viewing angle) to the east. The B5 image shows great detail of the cloud shock and closely resemble the [O III] filaments, but with an added “tail” extending to the southeast. The main body of the cloud shock as viewed in B5 is likely composed of C IV and O III] emission while the “tail” may be an example of a slow shock in a neutral medium and have an enhanced two-photon flux (Dopita, Binette, & Schwartz, 1982). The shock velocity in the cloud is quoted by Fesen et al. as  $<60 \text{ km s}^{-1}$  though this is based on the identification of the western segment as a reverse shock. Given the bright [O III] and B5 emission

in the cloud shock, it seems more likely that the cloud shock is similar to other structures to the north where shock velocities are thought to be more nearly  $140 \text{ km s}^{-1}$ .

There is a general increase in signal in the northern half of the SE FUV field (Figure 7c). It is unclear whether this is primarily due to the background “measles” noted in §2 or if this represents diffuse, hot gas emitting C IV as is seen in the halo around the central knot of XA. There is very faint emission seen in both  $\text{H}\alpha$  and [O III] in the area which could represent a region of more nearly face-on emitting gas.

## 5. Concluding Remarks

The UIT B5 band, although broader than ideal for SNR observations, provides a unique FUV spectral window. Under some conditions, the B5 bandpass provides images of radiative filaments overrun by very high-speed shocks. Under other conditions, B5 observes nonradiative filaments at the extreme front edge of SNR blast waves. Combined with other image and spectral data, the B5 band can provide unique insights into complex, difficult-to-model shock phenomena such as C IV resonance scattering and shock completeness.

In nonradiative filaments, B5 flux comes from a mixture of C IV as it ionizes up and two-photon emission from preshock neutral hydrogen. In general, nonradiative filament morphology is very similar in B5 and  $\text{H}\alpha$ , implying that two-photon emission, originating in the same regions as  $\text{H}\alpha$ , is the primary contributor to the B5 images. One unique capability of B5 imaging is its ability to capture nonradiative shocks in ionized media. We see one example of such in Figure 6c where a nonradiative shock is faintly seen in C IV and He II.

Radiative filaments usually show good correlation between B5 and [O III] morphology, suggesting that B5 flux arises in ions with similar excitation energies such as C IV. Existing models for simple, complete shocks indicate the same origin.

However, existing FUV spectra complicate this picture, indicating that these regions should be dominated by two-photon flux which we would expect to follow more closely the  $\text{H}\alpha$  morphology. Observational selection restricts detailed spectral information to only the very brightest knots and filaments. Presumably, these bright regions also suffer the greatest resonance scattering in C IV  $\lambda 1550$ , decreasing its observed flux; in fact, DBR found unexpectedly strong resonance scattering even away from the bright filaments and knots. Despite this, morphological similarities between B5 and [O III] in radiative filaments strongly suggest that, at least away from the brightest filaments and cloud cores, B5 flux is dominated by C IV.

**Acknowledgements** The authors wish to thank John Raymond for valuable discussions and the use of unpublished HUT data. We would also like to thank an anonymous referee for several valuable suggestions including using FUV images to trace nonradiative filaments through ionized

regions. Funding for the UIT project has been through the Spacelab Office at NASA headquarters under project number 440-551.

## REFERENCES

- Arendt, R.G., Dwek, E., & Leisawitz, D. 1992, *ApJ*, 400, 562
- Bedogni, R. & Woodward, P. R. 1990, *A&A*, 231, 481
- Benvenuti, P., Dopita, M., & D’Odorico, S. 1980, *ApJ*, 238, 601
- Blair, W. P., et al. 1991, *ApJ*, 379, L33
- Blair, W. P., Sankrit, R., Raymond, J. C. & Long, K. S., 1999, *AJ*, 118, 942
- Chevalier, R. A., Kirshner, R. P., & Raymond, J. C. 1980, *ApJ*, 235, 186
- Chevalier, R. A., & Raymond, J. C. 1978, *ApJ*, 225, L27
- Cornett, R. H., et al. 1992, *ApJ*, 395, L9
- Danforth, C. W., Blair, W. P., & Raymond, J. C. 2000, in prep. (DBR)
- Dopita, M. A., Binette, L., & Schwartz, R. D. 1982, *ApJ*, 261, 183
- Dopita, M. A., Binette, L. & Tuohy, I. R., 1984, *ApJ*, 282, 142
- Fesen, R. A., Blair, W. P., & Kirshner, R. P. 1982, *ApJ*, 262, 171
- Fesen, R. A., Kwitter, K. B. & Downes, R. A. 1992, *AJ*, 104, 719
- Graham, J. R., Levenson, N. A., Hester, J. J., Raymond, J. C., & Petre, R. 1995, *ApJ*, 444, 787
- Green, D. A. 1990, *AJ*, 100, 1927
- Hartigan, P., Raymond, J. C., & Hartmann, L., 1987, *ApJ*, 316, 323 (HRH)
- Hester, J. J., & Cox, D. P., 1986, *ApJ*, 300, 675
- Hester, J. J. 1987, *ApJ*, 314, 187
- Hester, J. J., Raymond, J. C., & Danielson, G. E. 1986, *ApJ*, 303, L17
- Hester, J. J., Raymond, J. C., & Blair, W. P. 1994, *ApJ*, 420, 721
- Innes, D. E. 1992, *A&A*, 256, 660
- Leahy, D. A., Roger, R. S., & Ballantyne, D. 1997, *AJ*, 114, 2081

- Levenson, N. A., Graham, J. R., Hester, J. J., & Petre, R. 1996, ApJ, 468, 323
- Levenson, N. A., et al. 1997, ApJ, 484, 304
- Levenson, N. A., Graham, J. R., Keller, L. D., & Richter, M. J. 1998, ApJS, 118, 541
- Long, K. S., et al. 1992, ApJ, 400, 214
- Miller, J. S. 1974, ApJ, 189, 239
- Nussbaumer, H., & Schmutz, W. 1984, A&A138, 495
- Osterbrock, D. S., 1989, “*Astrophysics of Gaseous Nebulae and Active Galactic Nuclei*”, Mill Valley, CA, University Science Books
- Raymond, J. C. 1979, ApJS, 39, 1
- Raymond, J. C., Davis, M., Gull, T. R., & Parker, R. A. R. 1980a, ApJ, 238, L21
- Raymond, J. C., Black, J. H., Dupree, A. K., Hartmann, L., & Wolff, R. S. 1980b, ApJ, 238, 881
- Raymond, J. C., Black, J. H., Dupree, A. K., Hartmann, L., & Wolff, R. S. 1981, ApJ, 246, 100
- Raymond, J. C., Blair, W. P., Fesen, R. A. & Gull, T. R. 1983, ApJ, 324, 869
- Raymond, J. C., et al. 1988, ApJ, 324, 869
- Scoville, N. Z., Irvine, W. M., Wannier, P. G., & Predmore, C. R. 1977, ApJ, 216, 320
- Smith, E. P., et al. 1996, ApJS, 104, 287
- Stecher, T. P., et al. 1992, ApJ, 395, L1
- Stecher, T. P., et al. 1997, PASP, 109, 584
- Stone, J. M., & Norman, M. L., 1992, ApJ, 390, L17
- Szentgyorgyi, A. H., Raymond, J. C., Hester, J. J., & Curiel, S. 2000, ApJ, in press
- Treffers, R. R. 1981, ApJ, 250, 213



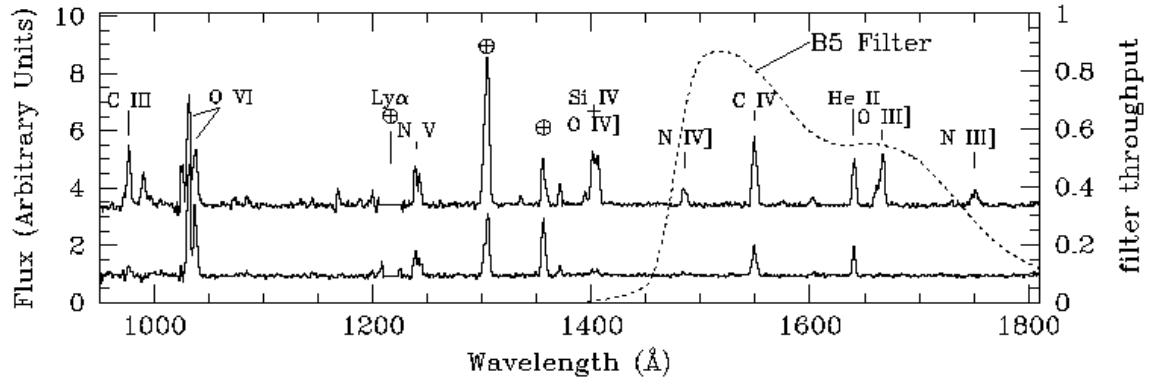


Fig. 1.— Two typical UV spectra of SNR filaments. The top, a radiative filament (Blair et al. 1991), shows lines of many different ions. The bottom, a nonradiative filament (Long et al. 1992), shows lines of only the highest ionization species. The dashed curve superimposed on the two spectra represents the throughput of UIT's B5 filter as a function of wavelength.

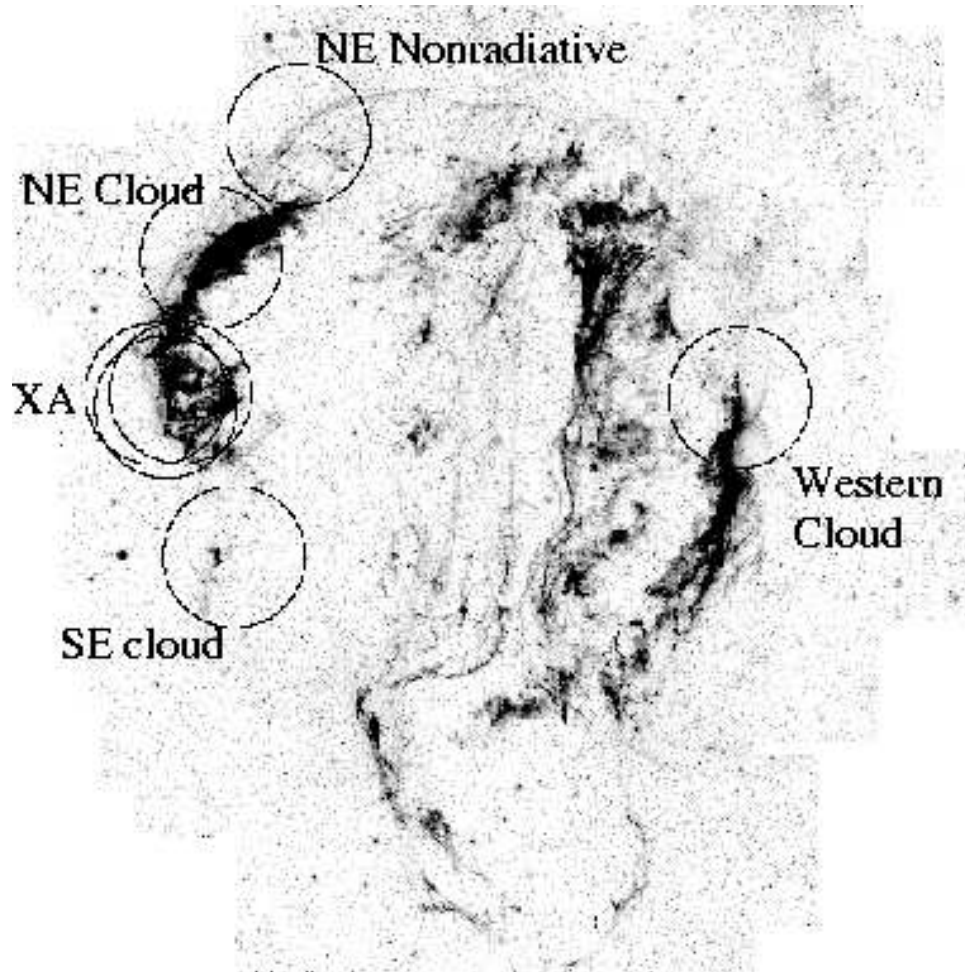


Fig. 2.— An  $H\alpha$  mosaic of the entire Cygnus Loop (courtesy Levenson et al. 1998) with the 40' UIT fields superimposed and labeled.

Fig. 3.— The Western Cloud as viewed in a)  $H\alpha$ , b)  $[O\ III]\lambda 5007$ , c) B5, and d) the ROSAT High Resolution Imager (HRI). All bands show a bright north-south radiative complex similar to that seen in the Northeast Cloud (Figure 5) but with apparently simpler geometry. Two bright, parallel filaments suggest two points of tangency to our line of sight. In  $H\alpha$  (a) and B5 (c) we also see a nonradiative filament diverging to the northwest of the bright radiative region. X-rays are seen behind this filament in (d). A reverse shock generates higher temperatures and brighter X-ray emission at the radiative region. With the exception of the nonradiative filament, the B5 and the  $[O\ III]$  (b) show a high degree of correlation, suggesting origin of the B5 flux in high-excitation ionic species. Each field is  $40'$  across. For Figures 3-7, both optical fields have been median-filtered with a 3-pixel ( $15''$ ) box. The HRI field has been smoothed with a 3-pixel gaussian. All fields are aligned and oriented with north at the top and east to the left. All image intensities are displayed logarithmically. (Please see attached file [uitfig3.jpg](http://www.pha.jhu.edu/~danforth/uit/uitfig3.jpg) or <http://www.pha.jhu.edu/~danforth/uit/> for full-resolution image.)

Fig. 4.— The Northeast Nonradiative Region, containing the classic nonradiative filaments, viewed as in Figure 3. The SN blast wave propagates through the atomic shell at  $v\sim 400\text{ km s}^{-1}$ . Thin filamentary emission arises from the preshock neutral fraction as it heats up, and is seen in  $H\alpha$  (a). Little or no emission is seen from this filament in  $[O\ III]$  (b). The shock is visible in B5 (c) through both two-photon processes (closely linked to  $H\alpha$  emission) and to a lesser extent through high-ionization species—in this case C IV. The ROSAT HRI image (d) shows the  $\sim 10^6\text{K}$  X-ray-emitting post-shock gas in a band behind the shock front. (Please see attached file [uitfig4.jpg](http://www.pha.jhu.edu/~danforth/uit/uitfig4.jpg) or <http://www.pha.jhu.edu/~danforth/uit/> for full-resolution image.)

Fig. 5.— The Northeast Cloud as viewed in Figure 3.  $H\alpha$  (a) shows smooth nonradiative filaments to the east of a more complex mass of radiative filaments.  $[O\ III]$  (b) shows a radiative filament structure complicated by line-of-sight coincidence of several emitting regions. The short B5 exposure (c) shows radiative structures well but is not deep enough to show the nonradiative filaments. The ROSAT image (d) shows that flux from hot gas behind the blast wave is considerably enhanced by the strongly decelerating shocks in the denser radiative region. (Please see attached file [uitfig5.jpg](http://www.pha.jhu.edu/~danforth/uit/uitfig5.jpg) or <http://www.pha.jhu.edu/~danforth/uit/> for full-resolution image.)

Fig. 6.— The XA region as viewed in Figure 3. This region displays a complex region of cloud-shock interactions, including dense, bright filaments whose C IV emission is apparently strongly affected by resonance scattering and a range of shock completeness (see Figures 9c and 10). (Please see attached file [uitfig6.jpg](http://www.pha.jhu.edu/~danforth/uit/uitfig6.jpg) or <http://www.pha.jhu.edu/~danforth/uit/> for full-resolution image.)

Fig. 7.— The South East Cloud viewed as in Figure 3. This small patch of emission is likely the tip of a much larger cloud early in the stages of shock interaction. B5 morphology (c) closely matches both  $H\alpha$  (a) and  $[O\ III]$  (b). The primary differences are faint features common only to B5 and  $H\alpha$ : the “tail” extending south of the cloud, and faint diffuse material—nonradiative blast wave filaments—in the southern half of the field. X-rays (d) show a region of emission much larger than the optical/UV cloud with a slight flux depression or “hole” in the center. (Please see attached file [uitfig7.jpg](http://www.pha.jhu.edu/~danforth/uit/uitfig7.jpg) or <http://www.pha.jhu.edu/~danforth/uit/> for full-resolution image.)

Fig. 8.— Three-color images of the Western Cloud (a), the Northeast Cloud (b), the XA Region (c) and the Southeast Cloud (d).  $H\alpha$  is in red, B5 emission in green and X-rays in blue. All intensities are displayed logarithmically and colors have been adjusted to best show spatial relationships. (Please see attached file [uitfig8.jpg](http://www.pha.jhu.edu/~danforth/uit/uitfig8.jpg) or <http://www.pha.jhu.edu/~danforth/uit/> for full-resolution image.)

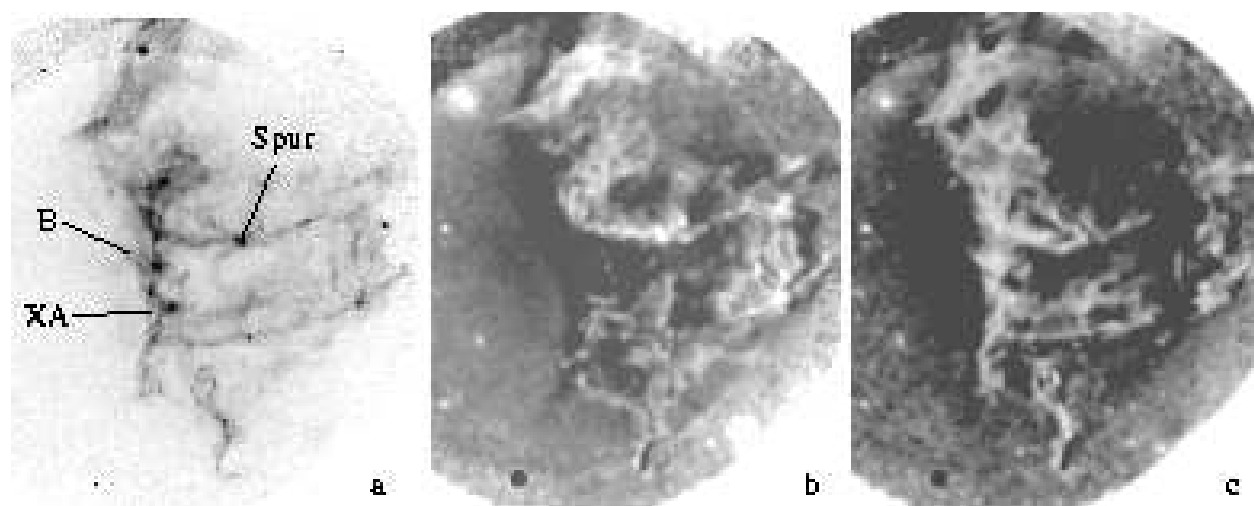


Fig. 9.— The effects of completeness and resonance scattering. a) UIT B5 image of the XA region. b) A “completeness map” generated by taking the ratio of B5 to  $H\alpha$ . Light areas represent more complete cooling while dark areas are less complete. Complete shocks emit predominantly two-photon emission in the B5 band while incomplete regions tend toward higher C IV contributions. c) “Saturation map” generated from B5 and [O III]. Dark regions show areas of higher resonance scattering of C IV.

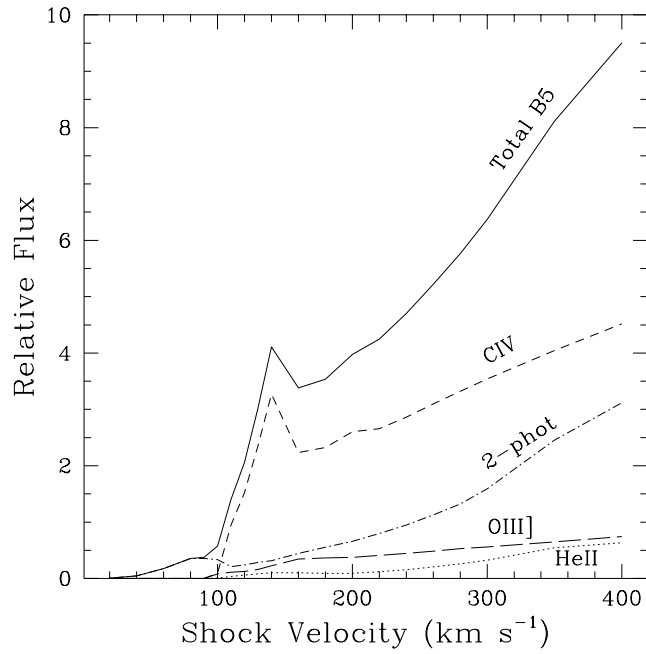


Fig. 10.— B5 flux as a function of velocity for the shock models of Hartigan, Raymond, & Hartmann (1987). The various dashed lines show the flux from selected ionic species multiplied by the B5 filter throughput, as a function of radiative shock velocity. The solid line is the total B5 flux calculated as a sum of  $0.80 \times \text{C IV} \lambda 1550$ ,  $0.55 \times \text{He II} \lambda 1640$ ,  $0.54 \times \text{O III] } \lambda 1665$ , and  $0.15 \times$  two-photon emission. These models hold only for complete, single-velocity shocks and do not take account of resonance scattering or other complications. In these models C IV emission dominates the B5 bandpass at all but the lowest velocities.

This figure "uitfig3.jpg" is available in "jpg" format from:

<http://arxiv.org/ps/astro-ph/0002005v1>

This figure "uitfig4.jpg" is available in "jpg" format from:

<http://arxiv.org/ps/astro-ph/0002005v1>

This figure "uitfig5.jpg" is available in "jpg" format from:

<http://arxiv.org/ps/astro-ph/0002005v1>



This figure "uitfig6.jpg" is available in "jpg" format from:

<http://arxiv.org/ps/astro-ph/0002005v1>

This figure "uitfig7.jpg" is available in "jpg" format from:

<http://arxiv.org/ps/astro-ph/0002005v1>

This figure "uitfig8.jpg" is available in "jpg" format from:

<http://arxiv.org/ps/astro-ph/0002005v1>